

Supplementary Information

Tuning the product selectivity of CO₂/H₂O co-electrolysis by CeO₂-modified proton-conducting electrolysis cells

Yongjian Ye^a, WonJun Lee^b, Junxian Pan^a, Xiang Sun^a, Mengzhen Zhou^a, Jiahui Li^a, Nian Zhang^c, Jeong Woo Han^{*b}, Yan Chen^{*a}

^a*School of Environment and Energy, National Engineering Laboratory for VOCs Pollution Control Technology and Equipment, South China University of Technology, Guangzhou, 510006, China*
E-mail: escheny@scut.edu.cn

^b*Computational Catalysis and Emerging Materials Laboratory, Pohang University of Science and Technology, Pohang, Gyeongbuk 37673, South Korea*
E-mail: jwhan@postech.ac.kr

^c*State Key Laboratory of Functional Materials for Informatics, Shanghai Institute of Microsystem and Information Technology, Chinese Academy of Sciences, Shanghai, 200050, China*

Experimental Sections

Material synthesis and PCECs preparation. BaZr_{0.1}Ce_{0.7}Y_{0.1}Yb_{0.1}O_{3-δ} (BZCYYb) was prepared using solid-state reaction. The weighed raw powders (BaCO₃, CeO₂, ZrO₂, Y₂O₃ and Yb₂O₃) were added with ball milling beads and ethanol to be ball-milled for 6 h, followed by sintering at 1150 °C for 10 h to form pure BZCYYb phase. The obtained materials were used for fabricating the electrolyte and fuel electrode support. PrBa_{0.5}Sr_{0.5}Co_{1.5}Fe_{0.5}O_{5+δ} (PBSCF) was synthesized by sol-gel method. Nitrate precursors (Pr(NO₃)₃·6H₂O, Ba(NO₃)₂, Sr(NO₃)₂, Co(NO₃)₂·6H₂O, and Fe(NO₃)₃·6H₂O) were stoichiometrically mixed and dissolved in deionized water. Ethylene diamine tetraacetic acid (EDTA) and citric acid (CA) were added in the solution as the complexing agents, and the molar ratio of total metallic ions, EDTA and CA was set to be 1:1:1.5. The PH of the solution was regulated by adding appropriate amount of ammonia. After evaporating the liquid solution at 80 °C, the gel formed, which was then heated in an oven at 300

°C for 10 h. The ashes were subsequently grounded and was calcined at 900 °C for 2 h to obtain pure PBSCF phase.

PCECs were assembled using a fuel electrode supported configuration. NiO, BZCYYb and starch (6:4:2) were ball-milled and then dry-pressed into pellets, which were then calcined at 800 °C for 2 h. Triethanolamine (TEA), polyethylene glycol (PEG-600), dioctyl phthalate (DOP), NiO and BZCYYb were mixed to form the electrolyte slurry. The electrolyte was dip-coating on the fuel electrode pellets and co-sintering at 1400 °C for 6 h. The oxygen electrode slurry was prepared by mixing PBSCF, BZCYYb and polyvinyl butyral (PVB)-terpineol at a mass ratio of 0.7:0.3:1, and was painted onto the electrolyte layer. The assembled cells were calcined at 950 °C for 2 h. The active area of the cell was 0.28 cm².

CeO₂-modified PCECs were prepared by an infiltration method. After assembling the fuel electrode supported cell, 0.1 M Ce(NO₃)₃ solution was infiltrated onto the fuel electrode surface. After calcination at 600 °C for 2 h, a thin layer of CeO₂ coating formed selectively onto the BZCYYb surface. Repeating the infiltration-calcination process until CeO₂ coating layer accounted for 3% of the cell mass.

Electrochemical measurements. Silver paste (DAD-87) and ceramic sealants (Ceramabond 552) were used to seal the PCECs to a glass tube. Silver grids were applied on both electrodes of PCECs as charge collectors. Upon being heated to 600 °C, the fuel electrode was fed with 50 sccm dry H₂ for 2 h to facilitate the reduction of NiO to Ni, while the oxygen electrode was exposed to air. The electrochemical performance of the cell was subsequently evaluated in fuel cell mode at 600 °C and 550 °C under identical gas compositions. At 550 °C, the gas composition was altered to initiate PCEC mode: the fuel electrode side was supplied with 2.6 sccm CO₂ + 50 sccm Ar and the oxygen electrode side with 100 sccm Ar containing 30% H₂O. This enabled the assessment of the electrochemical performance under PCEC operating conditions. Current-voltage (I-V) curves were obtained and constant voltage electrochemical impedance spectra (EIS) were measured in the frequency range from 100 kHz to 100 mHz at 550 °C. All electrochemical measurements were performed by Zahner Im6 System. The reaction product on the fuel

electrode side was analysed quantitatively by gas chromatography (GC9790II and GC9790Plus, Fuli Instruments).

Material Characterization. The crystal structures of all the samples were characterized by X-ray diffraction (XRD, Bruker D8 Advance, Germany) with Cu K α radiation. The microstructures of powder and cross-sectional view of PCECs were observed by scanning electron microscopy (SEM, SU8010, Japan) equipped with energy-dispersive spectroscopy (EDS). The surface chemistry was probed by X-ray photoelectron spectroscopy (XPS, ESCALAB 250Xi, USA) with Al K α (15 kV) X-ray radiation equipped with charge neutralization. CO₂ and CO temperature-programmed desorption (TPD, AutoChem1 II 2920) experiments were conducted from 50 to 900 °C at a rate of 10 °C min⁻¹ using pure He at a flow rate of 30 ml min⁻¹ as the carrier gas. Before the experiment started, all samples were purged with hydrogen at 600 °C for 2 h, and then cooled to 50 °C for TPD measurement. Ce M-edge and Ni L-edge soft X-ray absorption spectroscopy (sXAS) measurement for Ni/BZCYYb and CeO₂-modified Ni/BZCYYb were carried out at beamline 02B02 of the Shanghai Synchrotron Radiation Facility (SSRF). All the spectra were measured in the total electron yield (TEY) mode.

In situ diffuse reflectance infrared Fourier transform spectroscopy (*in situ* DRIFTS, Bruker 80v, Germany) was used to probe surface species on Ni/BZCYYb and CeO₂-Modified Ni/BZCYYb. The background data were collected in pure Ar at 550 °C (heating rate: 10 °C min⁻¹). A reaction gas (2.5% H₂ + 5% CO₂ + Ar) was introduced into the test chamber and the spectra were collected. The gas composition for DRIFT experiment was set to be the same value as we quantified for the electrolysis products under the current density of 1.25 A cm⁻² for the CeO₂-modified cell. As shown in Fig. 2e, when the current density is 1.25 A cm⁻², the hydrogen production rate and the total flow rate are 1.176 mL min⁻¹ (4.2 mL min⁻¹ cm⁻² with effective area of 0.28 cm² for the PCEC) and 52.6 mL min⁻¹, respectively, which corresponds to the hydrogen percentage of 2.23%. Therefore, to simulate the gas environment of the fuel electrode, we used 2.5% H₂ + 5% CO₂ as the gas composition both for the DRIFT and Raman spectra measurement.

In situ/Operando Raman spectroscopy (LabRAM HR 800) was conducted to investigate the intermediate species on the surface of fuel electrode. The model cells were fabricated using similar procedure reported in literature¹⁻³. First, Ni meshes were buried in the middle of the BZCYYb powder and pressed for 5 minutes at 5 MPa into pellets (13mm in diameter), which were then calcined at 1400 °C for 6 h. The obtained pellets were then polished with diamond suspensions until Ni meshes were exposed. Finally, Ag paste was painted into the opposite side of Ni/BZCYYb and dried at 180 °C. The prepared model cells were fixed in a Harrick environmental chamber with ceramic sealants. The *in situ* Raman test was carried out using a home-made test chamber with a structure shown in Fig. S13. The heating rate was set to be the 10 °C/min. After reaching 550 °C, voltages ranging from 1V to 1.6V were applied to the cell with Ni/BZCYYb or CeO₂-modified Ni/BZCYYb as the working electrode and the porous Ag as the counter electrode. To ensure that the cell reached a stable state, the holding time of each voltage was one hour. The composition of reacting gas for DRIFT and *in situ* Raman tests was set to be the same value as we quantified for the electrolysis products of CeO₂-modified cell under the current density of 1.25 A cm⁻² (2.5% H₂ + 5% CO₂).

Density functional theory (DFT) calculation. Density functional theory (DFT) calculations were performed using the Vienna Ab initio Simulation Package (VASP). The generalized gradient approximation (GGA) proposed by Perdew, Burke, and Ernzerhof (PBE) was used as the exchange-correlation energy functional. The cutoff energy for the plane wave was set to be 400 eV. Electronic occupancies were calculated by the Gaussian smearing with a smearing parameter of 0.05 eV. All structures were relaxed until the force on each atom was within 0.03 eV/Å on a force-based conjugate gradient algorithm. The GGA+U approach was used to take into account for on-site coulomb repulsion of f-orbitals on the Ce atoms with $U_{\text{eff}} = 5$ eV.

All calculations for CeO₂ (111) and BZCYYb (001) were performed with Monkhorst-Pack grids of $3 \times 2 \times 1$ and $2 \times 2 \times 1$ *k*-points. A vacuum thickness of 15 Å was used to exclude the artificial interaction between the periodic slab images. For BZCYYb, we used BO₂-terminated four layers of perovskite (001)

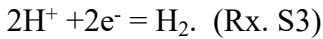
surface (Figure S16). For CeO₂, we used oxygen-terminated six layers of fluorite (111) surface (Fig. S17). For the bulk layer in the slab model, the bottom two layers were fixed.

The oxygen vacancy formation energies were calculated by the following equation.

$$E_{vf} = E_{oxide-defect} + \frac{1}{2}E_{O_2} - E_{oxide}$$

, where $E_{oxide-defect}$ and E_{oxide} are the total energies of BZCYYb and CeO₂ with and without oxygen vacancy, respectively. The reaction energy was calculated by the difference in the total energy of final and initial state at each elementary step.

Faradaic selectivity calculation: We calculated the selectivity based on Faradaic efficiency in the manuscript, which was similar to the methods used in several previous reports^{4, 5}. The conversion from CO₂ to CH₄ requires eight electron transfers, while CO₂ to CO and H₂ requires only two electron transfers, as shown in the following reactions:



The Faradic efficiency of products is calculated by the following equations (1):

$$FE_{CH_4} (\%) = \frac{8 \times V_{CH_4}}{1.34 \times 10^6 \times I \times F} \times 100\% , (Eq. S1)$$

$$FE_{CO} (\%) = \frac{2 \times V_{CO}}{1.34 \times 10^6 \times I \times F} \times 100\% , (Eq. S2)$$

$$FE_{H_2} (\%) = \frac{2 \times \dot{V}_{H_2}}{1.34 \times 10^6 \times I \times F} \times 100\% , (Eq. S3)$$

where I is the total current applied to the cell, and F is Faraday's constant (96485 C mol⁻¹). \dot{V}_{CH_4} , \dot{V}_{CO} and \dot{V}_{H_2} are the flow rates of CH₄, CO and H₂ in the exhaust gas stream, respectively. Product selectivity based on Faradaic efficiency is given by the following equations:

$$\text{CH}_4 \text{ Faradaic selectivity} = \frac{4 \times V_{\text{CH}_4}}{4 \times V_{\text{CH}_4} + V_{\text{CO}} + V_{\text{H}_2}} \times 100\% \quad , \text{ (Eq. S4)}$$

$$\text{CO Faradaic selectivity} = \frac{V_{\text{CO}}}{4 \times V_{\text{CH}_4} + V_{\text{CO}} + V_{\text{H}_2}} \times 100\% \quad , \text{ (Eq. S5)}$$

$$\text{H}_2 \text{ Faradaic selectivity} = \frac{V_{\text{H}_2}}{4 \times V_{\text{CH}_4} + V_{\text{CO}} + V_{\text{H}_2}} \times 100\% \quad , \text{ (Eq. S6)}$$

Considering the product selectivity comparison with the literature, we also adopted a general selectivity calculation method based on carbon balance, as shown in the following equations:

$$\text{CH}_4 \text{ selectivity} = \frac{\dot{V}_{\text{CH}_4}}{\dot{V}_{\text{CH}_4} + \dot{V}_{\text{CO}}} \times 100\% \quad , \text{ (Eq. S7)}$$

$$\text{CO selectivity} = \frac{\dot{V}_{\text{CO}}}{\dot{V}_{\text{CH}_4} + \dot{V}_{\text{CO}}} \times 100\% \quad , \text{ (Eq. S8)}$$

As shown in the Table S1, Faradaic selectivity and carbon-balance selectivity are similar. To reflect the current contribution to all products, we adopted a selectivity calculation method based on Faradaic efficiency in the manuscript.

Table S1. Comparison of CH₄ selectivity of CeO₂-modified PCEC based on faradaic efficiency with the one based on carbon balance under different current densities.

Current density (mA cm ⁻²)	Faradaic selectivity (%)	Carbon-balance Selectivity (%)
178	3.4	2.7
535	3.5	3
892	15.9	16
1250	16.8	17.3

Long-term stability test:

We found that the stability of the PBSCF oxygen electrode under the function condition of our cell (30% steam) is greatly challenging, which impacted the stability of the whole system. To show the evolution of the oxygen electrode more clearly, we carried an H₂O electrolysis test (with the fuel electrode exposed to pure Ar gas) at 600 °C. After ~100 hours of electrolysis at a current density of 500 mA cm⁻², an increase of 70 mV was exhibited by the voltage. Considering that the fuel electrode is stable in produced hydrogen gas environment, such degradation indicates the unsatisfied stability of the oxygen electrode under high steam condition. Our previous work found that La_{0.8}Sr_{0.2}CoO_{3-δ} (LSC) nanofibers have a compressive strain along the ab plane and less distorted CoO₆ octahedron than LSC powder sample, resulting in higher stability at high temperature⁶. Adapting similar strategy, we fabricated PBSCF nanofibers as oxygen electrode and found the nanostructured oxygen electrode exhibited better stability, which is likely due to the suppression of Ba and Sr segregation and improved gas diffusion. Using PBSCF nanowire as the oxygen electrode and 3% CeO₂-modified Ni/BZCYYb as fuel electrode, we further tested the H₂O/CO₂ co-electrolysis performance of the cell. As shown in Fig. S9, the electrolysis voltage showed negligible changes for a duration of 100 hours. The produced CH₄ flow rate is also stable, and is similar to what we obtained for the cells with PBSCF powder oxygen electrode under the same operation condition. SEM tests revealed that, after the long-term stability testing, the electrolyte remained well-connected to both the nanowire oxygen and fuel electrode (Fig. S9a), with no significant changes in the microstructure of the PBSCF nanofiber oxygen electrode (inset figure in Fig. S9b) and the fuel electrode. These results demonstrate the CeO₂-modified Ni/BZCYYb fuel electrode are stable for catalyzing the CO₂ hydrogenation reaction.

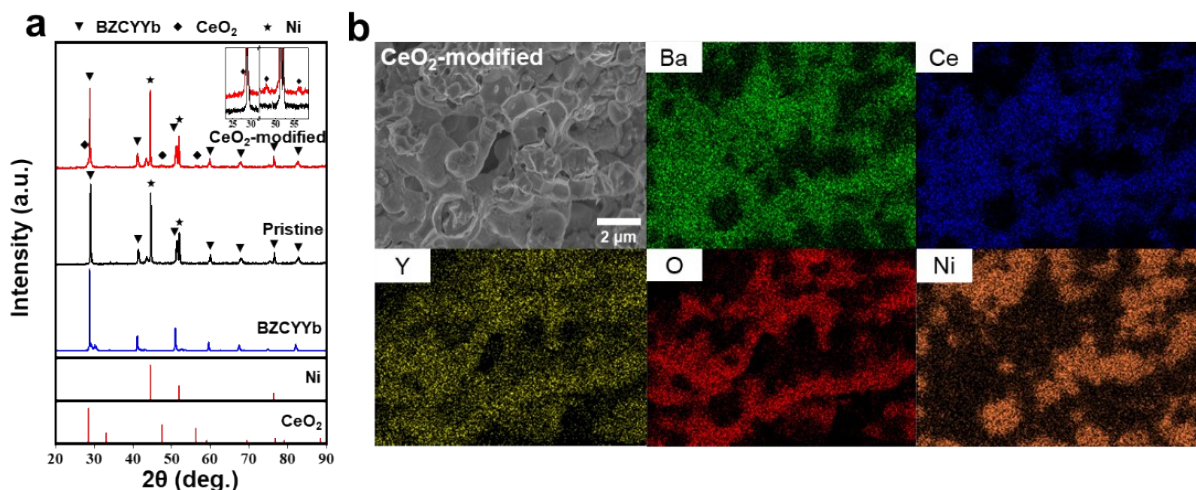


Fig. S1. Characterization of PCECs fuel electrode. **(a)** XRD patterns of BZCYYb powder, pristine Ni/BZCYYb electrode and CeO₂-modified Ni/BZCYYb electrode. The inset showed the enlarged patterns of the pristine and CeO₂-modified electrode with the CeO₂ peaks marked with diamond markers. The peak position of Ni metal and CeO₂ are also shown in the figure with red line. **(b)** SEM image and EDS element mapping of 3% CeO₂-modified electrode.

Text S1: Impact of CeO₂ coverage on the CO₂/H₂O co-electrolysis performance

In addition to 3% CeO₂, which we reported in the main text of the manuscript, two additional CeO₂ loading, 1% and 5% CeO₂, were impregnated onto the Ni/BZCYYb electrodes surface. Fig. S2 showed the XRD patterns of Ni/BZCYYb electrodes with different CeO₂ loading. The characteristic peak of CeO₂ in the XRD pattern increased with the increase of impregnation amounts, indicating that we successfully synthesized Ni/BZCYYb electrode with various CeO₂ loading.

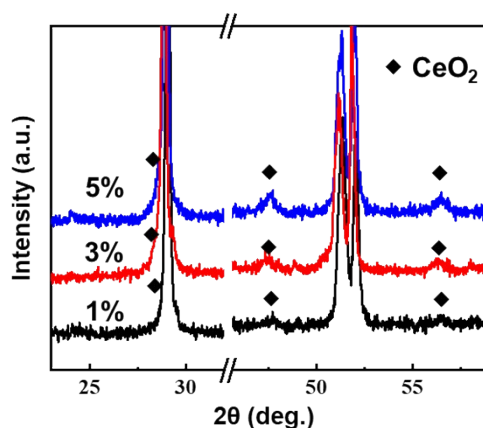


Fig. S2. XRD patterns of Ni/BZCYYb fuel electrodes with different CeO₂ impregnation amounts.

The morphology and chemical composition of Ni/BZCYYb electrodes with different CeO₂ loading were analyzed by scanning electron microscopy (SEM) and energy-dispersive spectroscopy (EDS), as shown in the Fig. S3-4. For the 1% CeO₂-modified fuel electrode, CeO₂ was mainly distributed on top of BZCYYb surface (Fig. S3), which was similar to the 3% CeO₂-modified fuel electrode (Fig. S1b). For the 5% CeO₂-modified fuel electrode, as shown in Fig. S4, the distribution area of Ce and O elements partly overlapped with that of Ni elements, and the brightness of Ni elements at the overlapping regions decreases significantly. This suggest that, when impregnated CeO₂ exceeded certain amount, a part of CeO₂ was deposited onto Ni surface.

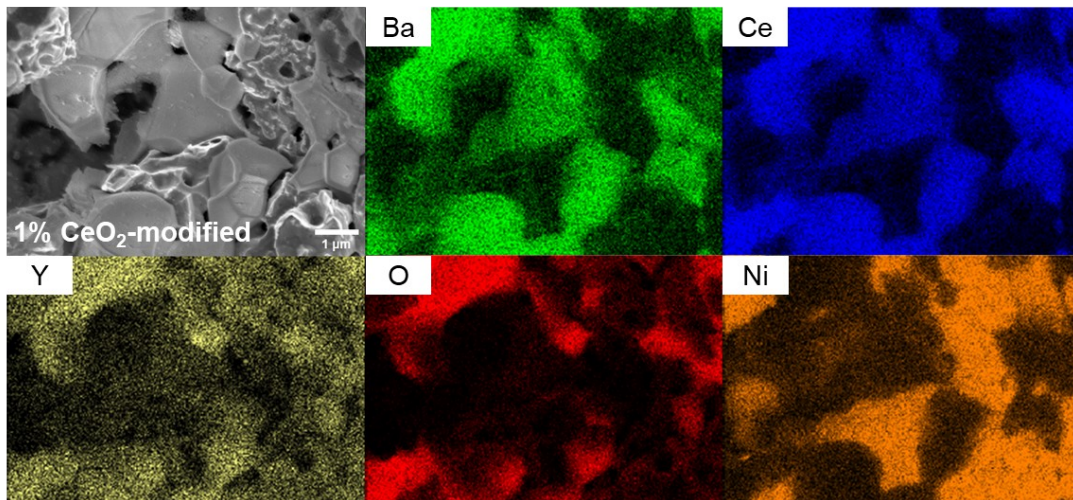


Fig. S3. SEM image and EDS element mapping of 1% CeO₂-modified electrode.

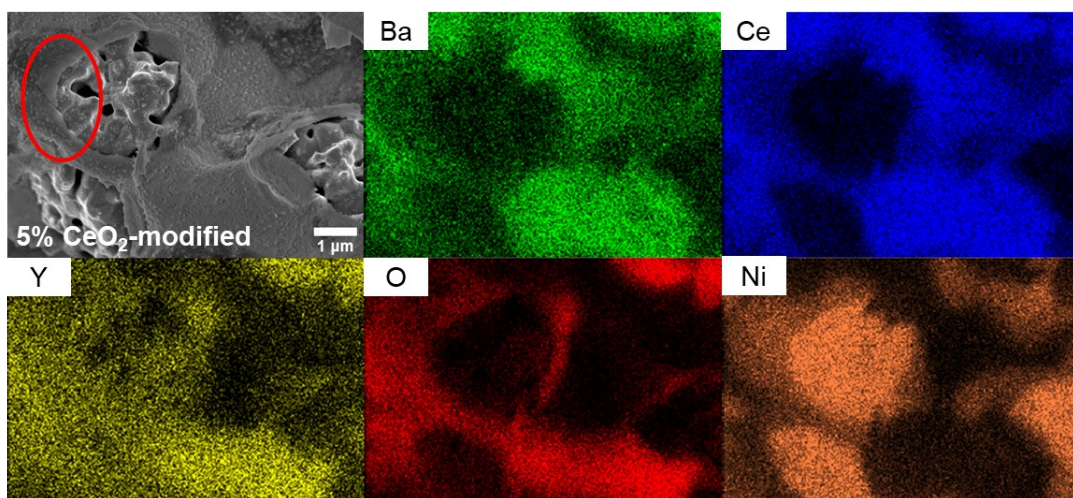


Fig. S4. SEM image and EDS element mapping of 5% CeO₂-modified electrode.

The current-voltage (I-V) curves of CO₂/H₂O co-electrolysis for the pristine cell, and the cells modified by 1%, 3%, and 5% CeO₂ were shown in Fig. S5. The 1% CeO₂-modified PCEC showed very similar performance as pristine PCEC, indicating that very small amount of CeO₂ modification did not introduce significantly changes in the electrolysis performance. The 5% CeO₂-modified PCEC, on the other hand, showed worse performance than the pristine cell. The CeO₂ itself is not a good proton conductor. Therefore, when too much CeO₂ is impregnated onto the Ni/BZCYYb surface, it may block the transport of proton to the surface and suppress the hydrogenation reaction of CO₂ on the surface. These results imply that there was an optimal amount of CeO₂ that needs to modify the Ni/BZCYYb surface to improve the co-electrolysis performance of the cell.

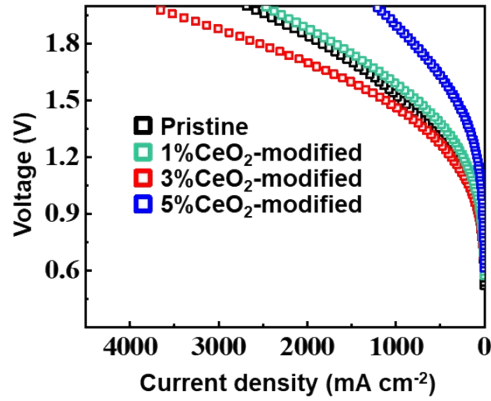


Fig. S5. Current-voltage (I-V) curves in 5% CO₂ at 550 °C. Inlet gas composition in fuel electrode: 2.6 sccm CO₂ + 50 sccm Ar; Oxygen electrode: 100 sccm Ar with 30% H₂O.

Text S2: Changes in the electrolyt transport characteristics induced by current density

Fick's first law can be used to calculate the change of steam pressure near the oxygen electrode surface ($C_{\text{H}_2\text{O}}^0$) at the interface of oxygen electrode and electrolyte ($C_{\text{H}_2\text{O}}^*$) during electrolysis^{7, 8}. The diffusion flux of steam is defined as:

$$J_{\text{diff}} = \frac{j}{nF} = -D_{\text{H}_2\text{O}}^{\text{eff}} \frac{C_{\text{H}_2\text{O}}^* - C_{\text{H}_2\text{O}}^0}{\delta}, \quad (1)$$

where j represents the current density, n is the charge transfer number ($n = 2$ for H_2O), F is Faraday's Constant ($96485 \text{ s A mol}^{-1}$), $D_{\text{H}_2\text{O}}^{\text{eff}}$ is the effective diffusivity of steam within the oxygen electrode, $C_{\text{H}_2\text{O}}^*$ (mol cm^{-3}) is the steam concentration at the interface between electrolyte and oxygen electrode, $C_{\text{H}_2\text{O}}^0$ is the steam concentration in the gas phase near the oxygen electrode surface. As current density increases, $C_{\text{H}_2\text{O}}^*$ near the electrolyte and electrode interface deviates more apparently from the steam pressure in the gas phase, which further leads to the changes in the transport characteristics of the electrolyte. On the other hand, as the current density increases to certain levels, the hole concentration and transfer number increase noticeably, suggesting increase in the electronic conductivity and the leakage of the electrolyte^{8, 9}. Our previous work as well as many literatures have reported the decreased of electrolysis performance due to the electrolyte leaking under high current density¹⁰⁻¹³. Therefore, we limited the current density used in this work to 1250 mA/cm^2 to prevent noticeable electronic conductivity in the protonic conduction electrolyte.

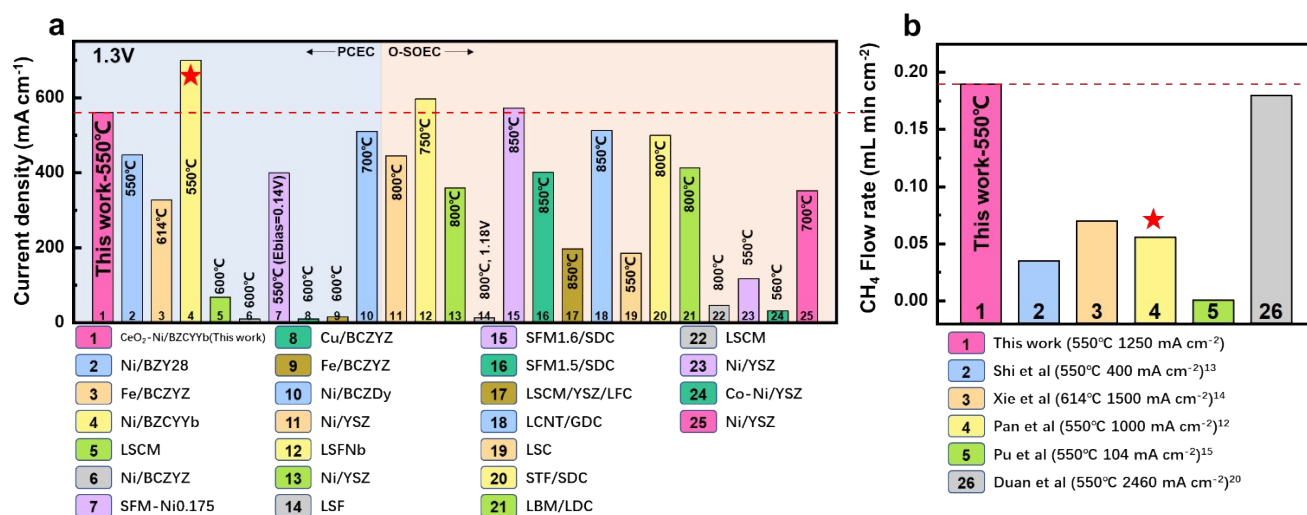


Fig. S6. (a) Comparison of the current density at 1.3V for CeO₂-modified Ni/BZCYYb electrode with those for other electrodes without noble metal catalysts in the H₂O/CO₂ co-electrolysis reaction^{12-19, 21-34}. (b) Comparison of the CH₄ production rate in the H₂O/CO₂ co-electrolysis reaction using PCEC with CeO₂-modified Ni/BZCYYb electrode with those for other electrodes^{12-15, 20}. The numbers in the figure correspond to the works listed in Table S2. Asterisks mark the work of Pan et al.¹².

Table S2. Comparison of the current density and selectivity of CeO₂-modified Ni/BZCYYb electrode with those for other electrodes without noble-metal catalysts for the H₂O/CO₂ co-electrolysis reaction and CH₄ selectivity.

Fuel electrode (gas composition)	Electrolyte	Oxygen electrode (gas composition)	Temperature	Current density for 1.3V	CH ₄ production rate (mL min ⁻¹ cm ⁻²)	Number	Reference
PCEC							
CeO ₂ -Ni/BaCe _{0.7} Zr _{0.1} Y _{0.1} Yb _{0.1} O _{3-δ} (5% CO ₂ +Ar)	BaCe _{0.7} Zr _{0.1} Y _{0.1} Yb _{0.1} O _{3-δ}	PrBa _{0.5} Sr _{0.5} Co _{1.5} Fe _{0.5} O _{5+δ} /BaCe _{0.7} Zr _{0.1} Y _{0.1} Yb _{0.1} O _{3-δ} (30% H ₂ O+Ar)	550 °C	559 mA cm ⁻¹	0.19 (1250 mA cm ⁻²)	1	This work
Ni/BaZr _{0.2} Y _{0.8} O _{3-δ} (100% CO ₂)	BaZr _{0.2} Y _{0.8} O _{3-δ}	Sr ₂ Eu ₂ Fe _{1.8} Co _{0.2} O _{7-δ} /BaZr _{0.2} Y _{0.8} O _{3-δ} (10%+Air)	550 °C	447 mA cm ⁻¹	0.035 (400 mA cm ⁻²)	2	Shi et al. ¹³
Fe/BaCe _{0.5} Zr _{0.3} Y _{0.16} Zn _{0.04} O _{3-δ} (100% CO ₂)	BaCe _{0.5} Zr _{0.3} Y _{0.16} Zn _{0.04} O _{3-δ}	Ni/BaCe _{0.5} Zr _{0.3} Y _{0.16} Zn _{0.04} O _{3-δ} (3% H ₂ O+H ₂)	614 °C	327 mA cm ⁻¹	0.07 (1500 mA cm ⁻²)	3	Xie et al. ¹⁴
Ni/BaCe _{0.4} Zr _{0.4} Y _{0.1} Yb _{0.1} O _{3-δ} (5% CO ₂ +Ar)	BaCe _{0.4} Zr _{0.4} Y _{0.1} Yb _{0.1} O _{3-δ}	BaCo _{0.4} Fe _{0.4} Zr _{0.1} Y _{0.1} O ₃ - δ/BaCe _{0.4} Zr _{0.4} Y _{0.1} Yb _{0.1} O _{3-δ}	550 °C	700 mA cm ⁻¹	0.056 (1000 mA cm ⁻²)	4	Pan et al. ¹²
(La _{0.75} Sr _{0.25}) _{0.97} Mn _{0.5} Cr _{0.5} O _{3-δ} (100% CO ₂)	BaCe _{0.5} Zr _{0.3} Y _{0.2} O _{3-δ} - (Li, Na) ₂ CO ₃	(La _{0.75} Sr _{0.25}) _{0.97} Mn _{0.5} Cr _{0.5} O _{3-δ} (12% H ₂ O+Ar)	600 °C	68 mA cm ⁻¹	0.00086 (550 °C 104 mA cm ⁻²)	5	Pu et al. ¹⁵
Ni/BaCe _{0.5} Zr _{0.3} Y _{0.16} Zn _{0.04} O _{3-δ} (100% CO ₂)	BaCe _{0.5} Zr _{0.3} Y _{0.16} Zn _{0.04} O _{3-δ}	(La _{0.75} Sr _{0.25}) _{0.95} Mn _{0.5} Cr _{0.5} O _{3-δ} (5% H ₂ O+Ar)	600 °C	9.9 mA cm ⁻¹	/	6	Wu et al. ¹⁶
Sr ₂ Fe _{1.4} Mo _{0.5} O _{6-δ} - Ni _{0.175} (100% CO ₂)	BaCe _{0.4} Zr _{0.4} Y _{0.1} Yb _{0.1} O _{3-δ}	Ni/BaCe _{0.7} Zr _{0.1} Y _{0.1} Yb _{0.1} O _{3-δ} (20% H ₂ +Ar)	550 °C	400 mA cm ⁻¹ (E _{bias} =0.14V)	/	7	Liu et al. ¹⁷
Cu/ BaCe _{0.5} Zr _{0.3} Y _{0.16} Zn _{0.04} O _{3-δ} (100% CO ₂)	BaCe _{0.5} Zr _{0.3} Y _{0.16} Zn _{0.04} O _{3-δ}	Ni/ BaCe _{0.5} Zr _{0.3} Y _{0.16} Zn _{0.04} O _{3-δ} (3% H ₂ O+4.85% H ₂ +Ar)	600 °C	11.2 mA cm ⁻¹	/	8	E. Ruiz-Trejo et al. ¹⁸
Fe/ BaCe _{0.5} Zr _{0.3} Y _{0.16} Zn _{0.04} O _{3-δ} (100% CO ₂)				11.4 mA cm ⁻¹	/	9	
Ni/BaCe _{0.3} Zr _{0.5} Dy _{0.2} O _{3-δ} (48.5% CO ₂ +48.5% H ₂ +3% H ₂ O)	BaCe _{0.3} Zr _{0.5} Dy _{0.2} O _{3-δ}	Nd _{1.95} Ba _{0.05} NiO _{4+δ} / BaCe _{0.3} Zr _{0.5} Dy _{0.2} O _{3-δ}	700 °C	510 mA cm ⁻¹	/	10	Nikolay et al. ¹⁹
Ni/BaCe _{0.7} Zr _{0.1} Y _{0.1} Yb _{0.1} O _{3-δ} (5.5% CO ₂ +Ar)	BaCe _{0.7} Zr _{0.1} Y _{0.1} Yb _{0.1} O _{3-δ}	BaCo _{0.4} Fe _{0.4} Zr _{0.1} Y _{0.1} O _{3-δ} / BaCe _{0.7} Zr _{0.1} Y _{0.1} Yb _{0.1} O _{3-δ} (18% H ₂ O+Air)	550 °C	2460 mA cm ⁻¹	0.18	26	Duan et al. ²⁰
O-SOEC							

Ni/YSZ (10% CO ₂ +60%H ₂ +30%H ₂ O)	YSZ	LSM/YSZ (Air)	800 °C	445 mA cm ⁻¹	/	11	Chen et al. ²¹
La _{0.5} Sr _{0.5} Fe _{0.9} Nb _{0.1} O _{3-δ} (80% CO ₂ +20% H ₂ O)	La _{0.8} Sr _{0.2} Ga _{0.83} Mg _{0.17} O _{3-δ}	La _{0.5} Sr _{0.5} Fe _{0.9} Nb _{0.1} O _{3-δ} (Air)	750 °C	597 mA cm ⁻¹	/	12	Bian et al. ²²
Ni/Zr _{0.85} Y _{0.15} O _{2-δ} (49% CO ₂ +10% H ₂ +20% H ₂ O+21% CO)	Zr _{0.85} Y _{0.15} O _{2-δ}	La _{0.8} Sr _{0.2} MnO _{3-δ} /Zr _{0.85} Y _{0.15} O _{2-δ} (Air)	800 °C	360 mA cm ⁻¹	/	13	Zheng et al. ²³
La _{0.7} Sr _{0.2} FeO ₃ (40% CO ₂ +3% H ₂ O+He)	YSZ	LSM/YSZ (Air)	800 °C	13.8 mA cm ⁻¹ (E=1.18V)	/	14	Deka et al. ²⁴
Sr ₂ Fe _{1.6} Mo _{0.5} O _{6-δ} /Ce _{0.8} Sm _{0.2} O _{2-δ} (50% CO ₂ +50% H ₂ O)	La _{0.9} Sr _{0.1} Ga _{0.8} Mg _{0.2} O _{3-δ}	Sr ₂ Fe _{1.6} Mo _{0.5} O _{6-δ} /Ce _{0.8} Sm _{0.2} O _{2-δ} (Air)	850 °C	573 mA cm ⁻¹	/	15	Hou et al. ²⁵
Sr ₂ Fe _{1.5} Mo _{0.5} O _{6-δ} /Ce _{0.8} Sm _{0.2} O _{2-δ} (50% CO ₂ +50% H ₂ O)		Sr ₂ Fe _{1.5} Mo _{0.5} O _{6-δ} /Ce _{0.8} Sm _{0.2} O _{2-δ} (Air)		401 mA cm ⁻¹	/	16	
La _{0.75} Sr _{0.25} Mn _{0.5} Cr _{0.5} O _{3-δ} /ZrO ₂ -8%Y ₂ O ₃ /LaFe _{0.6} Co _{0.4} O ₃ (9% CO ₂ +20% H ₂ O+5% H ₂ +N ₂)	ZrO ₂ -8%Y ₂ O ₃	Pt (Air)	850 °C	197 mA cm ⁻¹	/	17	Khameneh et al. ²⁶
La _{0.43} Ca _{0.37} Ni _{0.06} Ti _{0.94} O ₃ /GDC (25% CO ₂ +25% H ₂ O+50% H ₂)	ScCeSZ	LSM/YSZ (Air)	850 °C	513 mA cm ⁻¹	/	18	Kyriakou et al. ²⁷
La _{0.6} Sr _{0.4} CoO ₃ (5.1% CO ₂ +5.3% H ₂ O+12.8% H ₂ +He)	GDC/YSZ	Ni/YSZ (Air)	550 °C	186 mA cm ⁻¹	/	19	Lo et al. ²⁸
Sr ₂ Ti _{0.8} Co _{0.2} FeO ₆ /Ce _{0.8} Sm _{0.2} O _{1.9} (50% CO ₂ +50% H ₂ O)	La _{0.9} Sr _{0.1} Ga _{0.8} Mg _{0.2} O _{3-δ}	Sr ₂ Ti _{0.8} Co _{0.2} FeO ₆ /Ce _{0.8} Sm _{0.2} O _{1.9} (Air)	800 °C	500 mA cm ⁻¹	/	20	Niu et al. ²⁹
La _{0.5} Ba _{0.5} MnO _{3-δ} /La _{0.4} Ce _{0.6} O _{2-δ} (86% CO ₂ +10% H ₂ O+4% CO)	La _{0.8} Sr _{0.2} Ga _{0.8} Mg _{0.2} O _{3-δ}	La _{0.5} Ba _{0.5} MnO _{3-δ} /La _{0.4} Ce _{0.6} O _{2-δ} (Air)	800 °C	413 mA cm ⁻¹	/	21	Gan et al. ³⁰
La _{0.75} Sr _{0.25} Mn _{0.5} Cr _{0.5} O _{3-δ} (40% CO ₂ +60% H ₂ O)	ZrO ₂ -8%Y ₂ O ₃	La _{0.6} Sr _{0.4} Co _{0.2} FeO ₆ O _{3-δ} (Air)	800 °C	46.7 mA cm ⁻¹	/	22	Ma et al. ³¹
Ni/YSZ (16.6% CO ₂ +16.7% H ₂ O+ H ₂)	Ga _{0.1} Ce _{0.9} O ₂	Sm _{0.5} Sr _{0.5} CoO ₃ /Ga _{0.1} Ce _{0.9} O ₂ (Air)	550 °C	118 mA cm ⁻¹	/	23	Baxter et al. ³²
Co-Ni/YSZ (30% CO ₂ +20% H ₂ O+ 30% H ₂)	YSZ	La _{0.6} Sr _{0.4} CoO ₃ /La _{0.6} Sr _{0.4} Co _{0.2} FeO ₆ O _{3-δ} (Air)	560 °C	32 mA cm ⁻¹	/	24	Patryk et al. ³³
Ni/3%YSZ (40% CO ₂ +40% H ₂ O+ 20%	3%YSZ	GDC/LSCF-GDC (Air)	700 °C	352 mA cm ⁻¹	/	25	Xi et al. ³⁴

H ₂)							
------------------	--	--	--	--	--	--	--

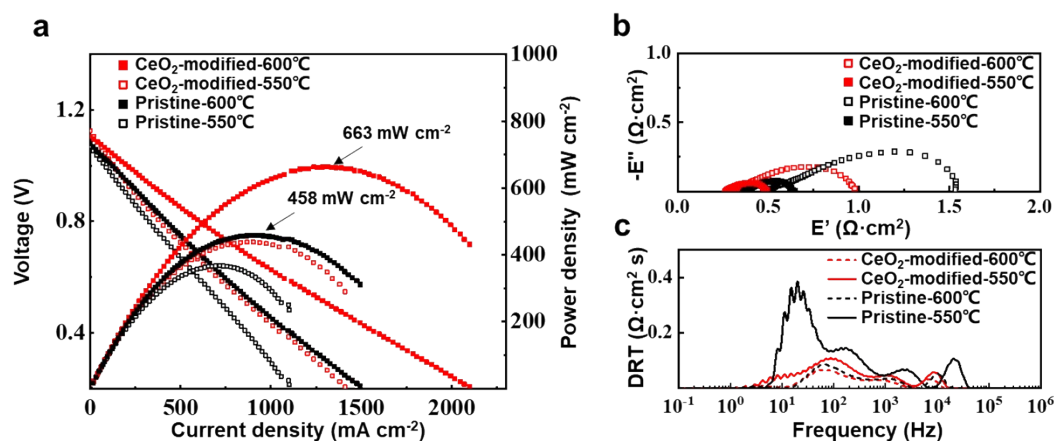


Fig. S7. Comparison between the different electrodes in fuel cell mode at 600 °C and 550 °C. **(a)** I-V/P curves; **(b)** impedance spectra; **(c)** distribution of relaxation times (DRT) analysis.

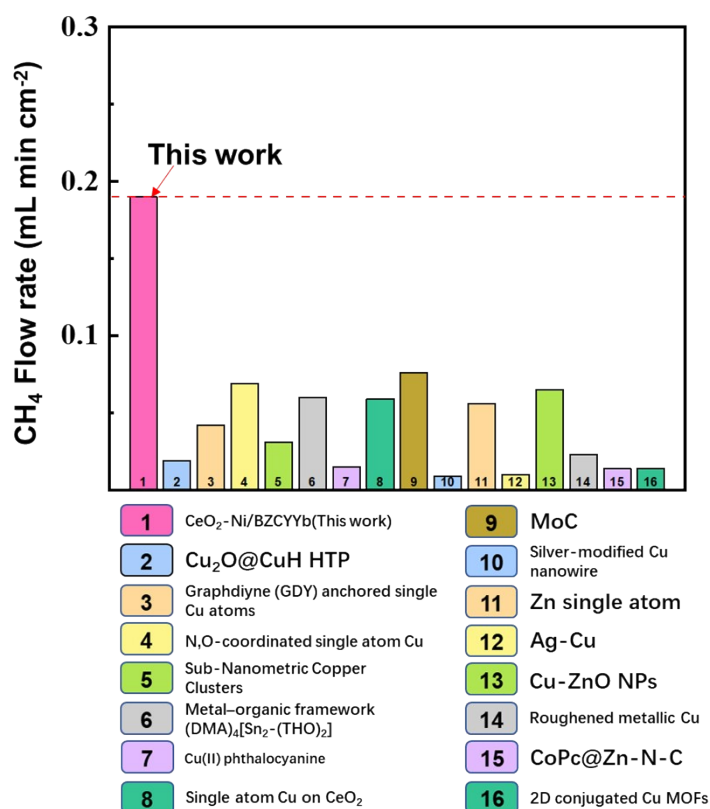


Fig. S8. Comparison of CH₄ flow rate for the CeO₂-modified PCEC in this work and state-of-the-art AEM electrolyzers³⁵⁻⁴⁹. The detailed function condition and reference are listed in Table S3.

Table S3. A detailed comparison of the parameters for CO₂ reduction performance and CH₄ flow rate between CeO₂-modified PCEC and the state-of-the-art AEM electrolyzers.

Catalyst	E[V vs. RHE]	Current density (mA cm ⁻²)	CH ₄ flow rate (mL min ⁻¹ cm ⁻²)	Reference
1. CeO ₂ -Ni/BZCYYb	1 (vs. OCP)	1250	0.19	This work
2. Cu ₂ O@CuH HTP ³⁵	-1.4	73	0.019	<i>Angew. Chem. Int. Ed.</i> , 2020, 59(52), 23641.
3. Graphdiyne (GDY) anchored single Cu atoms ³⁶	-1.3	36.36	0.042	<i>Angew. Chem. Int. Ed.</i> , 2022, 61(23): e202203569.
4. N,O-coordinated single atom Cu ³⁷	-1.14	78	0.069	<i>Nat. Commun.</i> , 2021, 12(1): 586.
5. Sub-Nanometric Copper Clusters ³⁸	-1	81.7	0.031	<i>Angew. Chem. Int. Ed.</i> , 2020, 59(43): 19054
6. Metal–organic framework (DMA) ₄ [Sn ₂ -(THO) ₂] ³⁹	-1.6	74.1	0.060	<i>Angew. Chem. Int. Ed.</i> , 2023: e202301767.
7. Cu(II) phthalocyanine ⁴⁰	-1.06	66	0.015	<i>Nat. Commun.</i> , 2018, 9(1): 415.
8. Single atom Cu on CeO ₂ ⁴¹	-1.8	58	0.059	<i>ACS Catal.</i> , 2018, 8(8): 7113.
9. MoC ⁴²	-0.9	89	0.076	<i>Adv. Energy Mater.</i> 2021, 11(24): 2100044.
10. Silver-modified Cu nanowire ⁴³	-1.4	9.1	0.009	<i>J. Am. Chem. Soc.</i> 2020, 142 (28):12119.

11. Zn single atom ⁴⁴	-1.15	85	0.056	<i>J. Am. Chem. Soc.</i> 2020, 142(29): 12563.
12. Ag-Cu ⁴⁵	-1.1	55	0.010	<i>Nat. Commun.</i> , 2019, 10(1): 3340.
13. Cu-ZnO NPs ⁴⁶	-1.4	70	0.065	<i>J. Am. Chem. Soc.</i> 2019, 141(50): 19879.
14. Roughened metallic Cu ⁴⁷	-1.2	62	0.023	<i>Nat. Commun.</i> 2018, 9(1): 925.
15. CoPc@Zn-N-C ⁴⁸	-1.24	44.3	0.014	<i>Angew. Chem. Int. Ed.</i> , 2020, 59(50): 22408
16. 2D conjugated Cu MOFs ⁴⁹	-1.5	78	0.014	<i>Angew. Chem., Int. Ed.</i> 2021, 60(30): 16409.

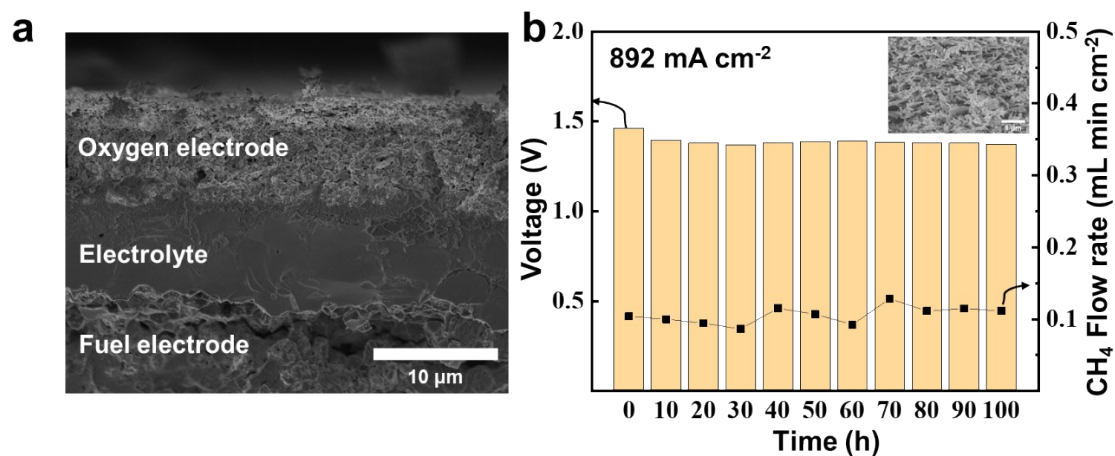


Fig. S9. (a) SEM image of the cell with CeO₂-modified BZCYYb fuel electrode and PBSCF nanowires oxygen electrode. (b) Long-term stability testing of the cell with CeO₂-modified BZCYYb fuel electrode

and PBSCF nanowires oxygen electrode at 550 °C at a current density of 892 mA cm⁻². The inlet gas of oxygen electrode was 50 sccm Ar gas with 30% H₂O. The inlet gas of fuel electrode was 52.6 sccm Ar gas with 5% CO₂. The voltage was continuously recorded and the CH₄ flow rate was calculated on the basis of a continuous measurement of the CH₄ production. The inset showed the structure of oxygen electrode nanofibers after long-term stability testing.

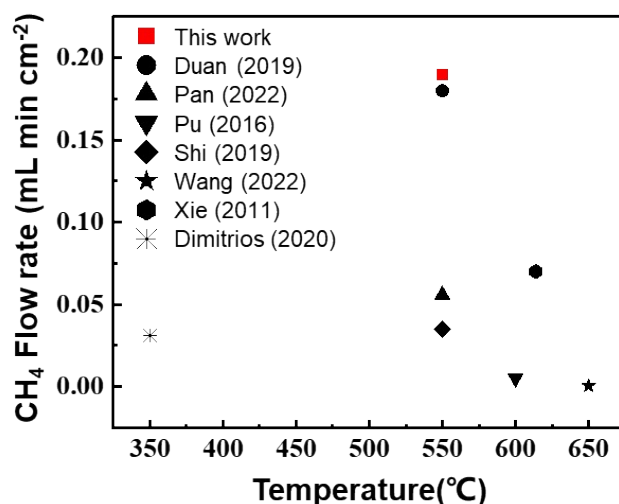


Fig. S10. The optimal function temperature and corresponding CH₄ flow rate for CO₂-H₂O co-electrolysis to produce CH₄ using PCEC reported in literature^{12-15, 20, 50, 51}.

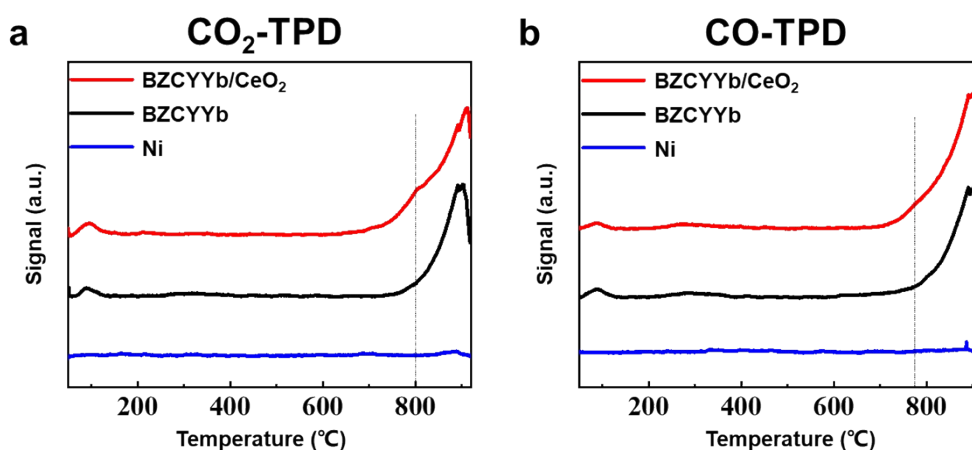


Fig. S11. (a) CO₂-TPD and (b) CO-TPD spectra of CeO₂/BZCYYb, BZCYYb and Ni samples, respectively.

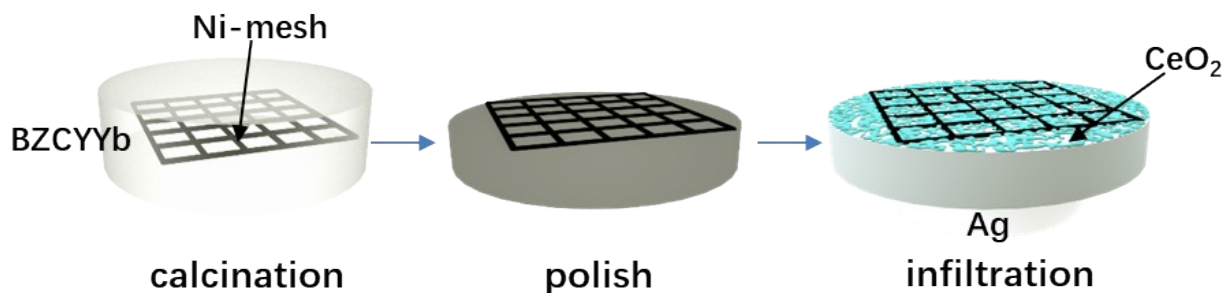


Fig. S12. Procedure of the model cell fabrication for *in situ* Raman spectroscopy measurement.

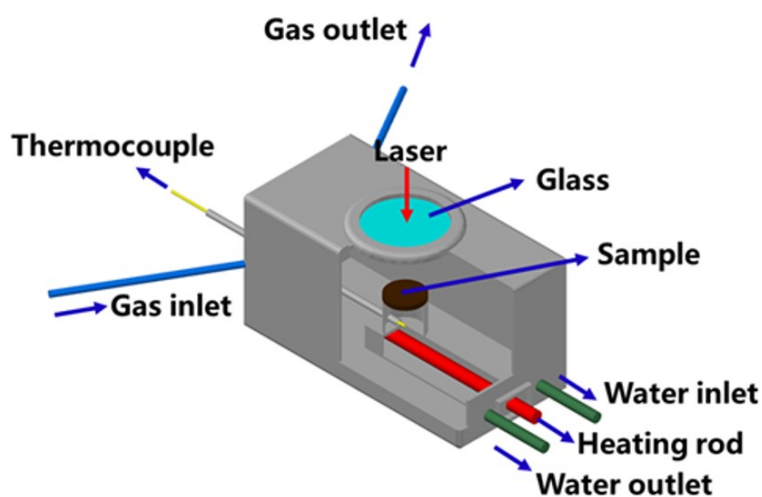


Fig. S13. Schematic of the Harrick environmental chamber used for the *in situ* Raman spectroscopy measurement.

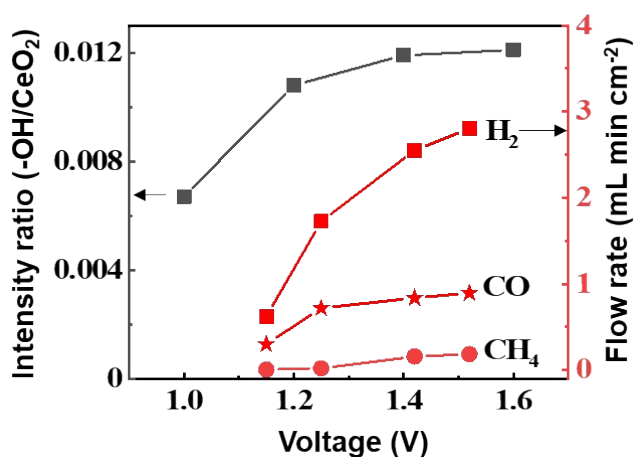


Fig. S14. Intensity ratio of surface hydroxyl (-OH) to CeO₂ F2g peak in the *in situ* Raman spectra in Fig. 4(b) and flow rate of reaction products (CH₄, CO, H₂) as a function of applied voltage for CeO₂-modified cell.

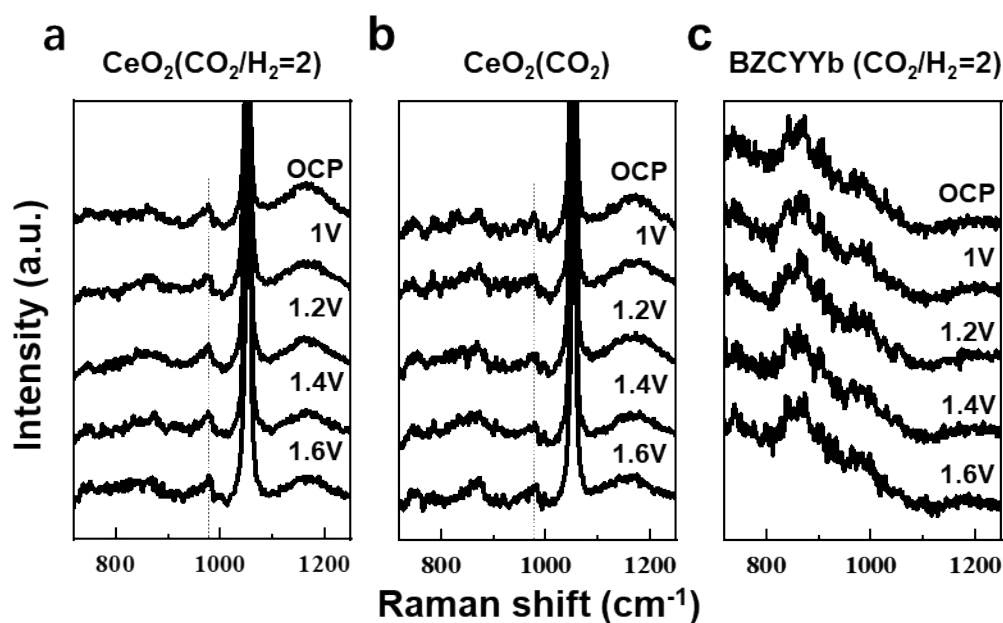


Fig. S15. In situ Raman spectra obtained **(a)** on top of CeO_2 faraway from the Ni/BZCYYb interface for the CeO_2 -modified samples in the mixture of CO_2 and H_2 (5% $\text{CO}_2 + 2.5\% \text{H}_2$), **(b)** on top of CeO_2 near the Ni/BZCYYb interface for the CeO_2 -modified samples in pure CO_2 environment at 550 °C, and **(c)** on top of BZCYYb near the Ni/BZCYYb interface for the pristine sample under applied potential ranging from 1 to 1.6V.

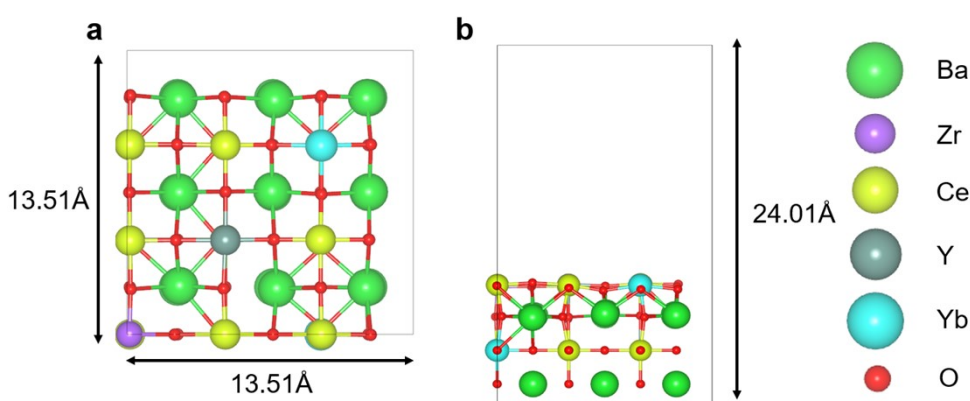


Fig. S16. **(a)** Top and **(b)** side views of DFT-optimized surface structures of BZCYYb (001). $\text{BaZr}_{1/9}\text{Ce}_{2/3}\text{Y}_{1/9}\text{Yb}_{1/9}\text{O}_3$ was used to approximately model the $\text{BaZr}_{0.1}\text{Ce}_{0.7}\text{Y}_{0.1}\text{Yb}_{0.1}\text{O}_{3-\delta}$ compound.

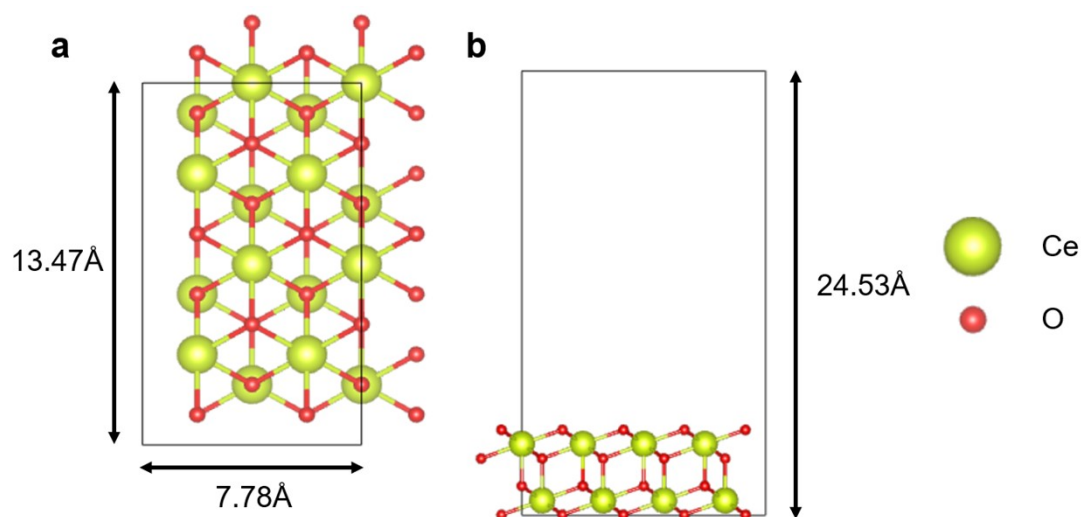


Fig. S17. (a) Top and (b) side views of DFT-optimized surface structures of CeO_2 (111).

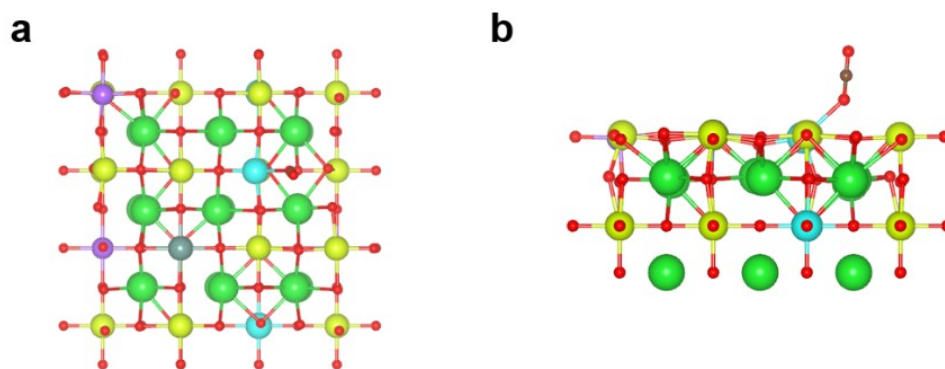


Fig. S18. (a) Top and (b) side views of DFT-optimized surface structures of BZCYYb (010) with CO adsorption. CO adsorption calculations were performed for 10 possible sites, perpendicular to lattice oxygen, cation (Zr, Y, Yb, Ce). CO was most stably adsorbed to Yb nearest lattice oxygen.

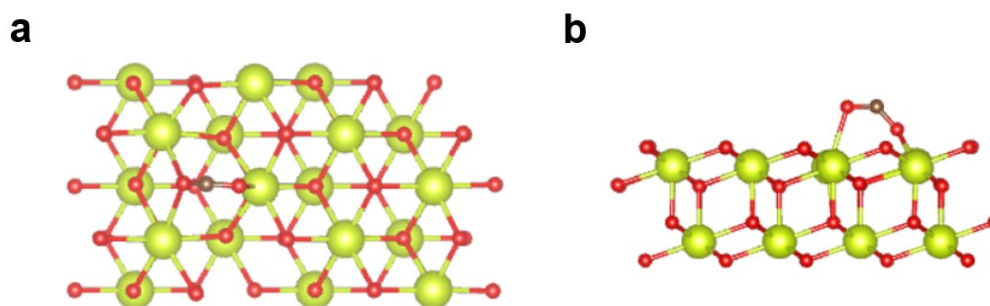


Fig. S19. (a) Top and (b) side views of DFT-optimized surface structures of CeO₂ (111) with CO adsorption. CO adsorption calculations were performed perpendicular to lattice oxygen, Ce, parallel to lattice oxygen-Ce. CO was most stably adsorbed parallel to lattice oxygen-Ce.

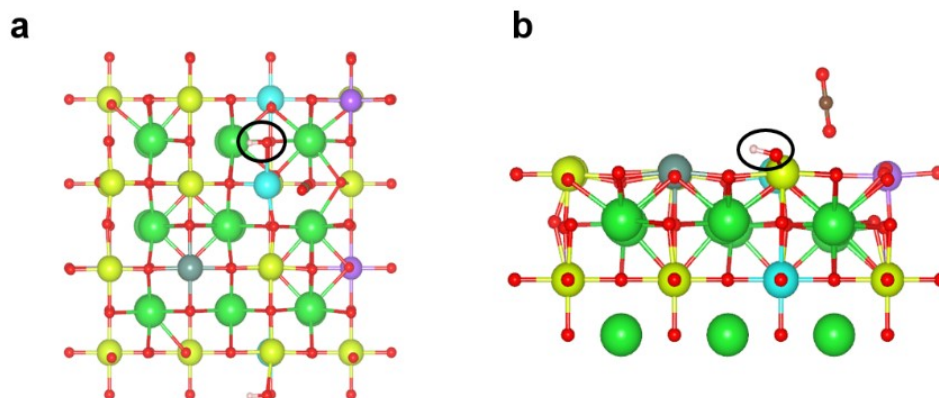


Fig. S20. (a) Top and (b) side views of DFT-optimized surface structures of BZCYYb (010) with protons adsorption (solid circle). Proton adsorption calculations were performed to lattice oxygen, cation (Zr, Y, Yb, Ce). Protons were most stably adsorbed on lattice oxygen nearest to CO*.

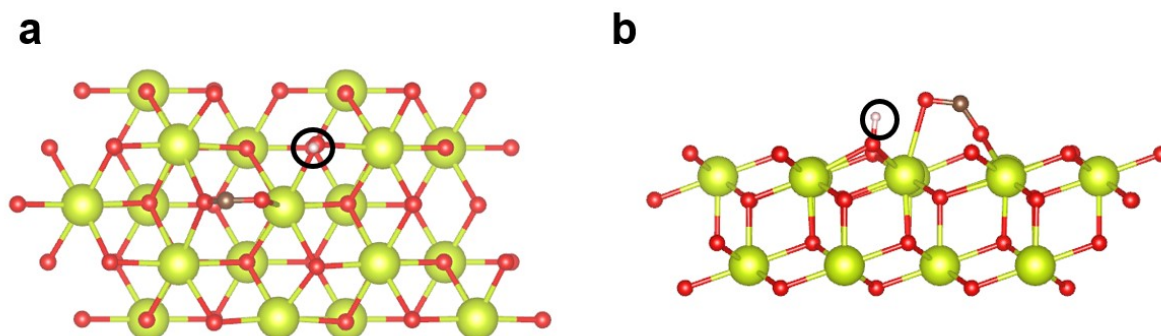


Fig. S21. (a) Top and (b) side views of DFT-optimized surface structures of CeO₂ (111) with proton adsorption (solid circle). Proton adsorption calculations were performed to lattice oxygen and Ce. Protons were most stably adsorbed on lattice oxygen nearest to CO*.

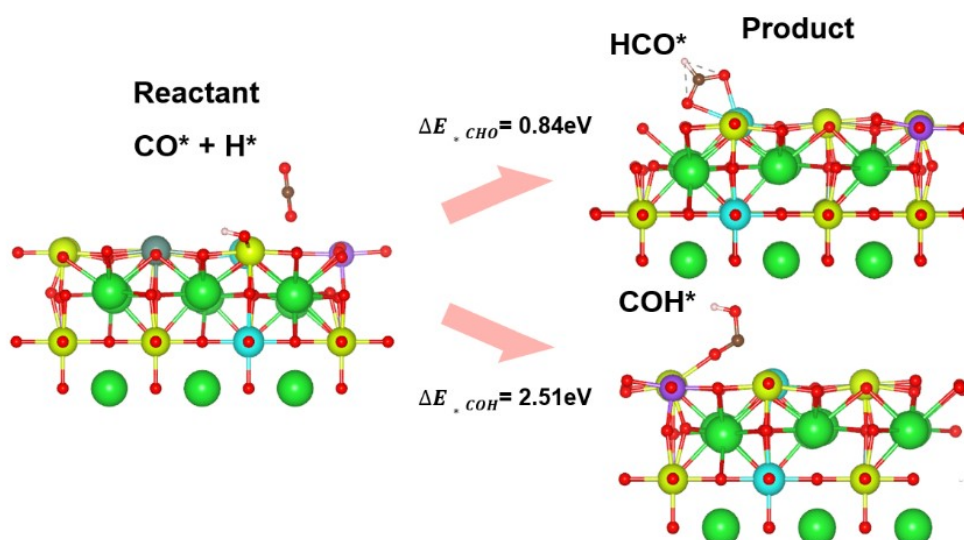


Fig. S22. CO hydrogenation energy on BZCYYb was calculated via the reaction energy of $\text{CO}^* + \text{H}^* \rightarrow \text{HCO}^*$ or COH^* .

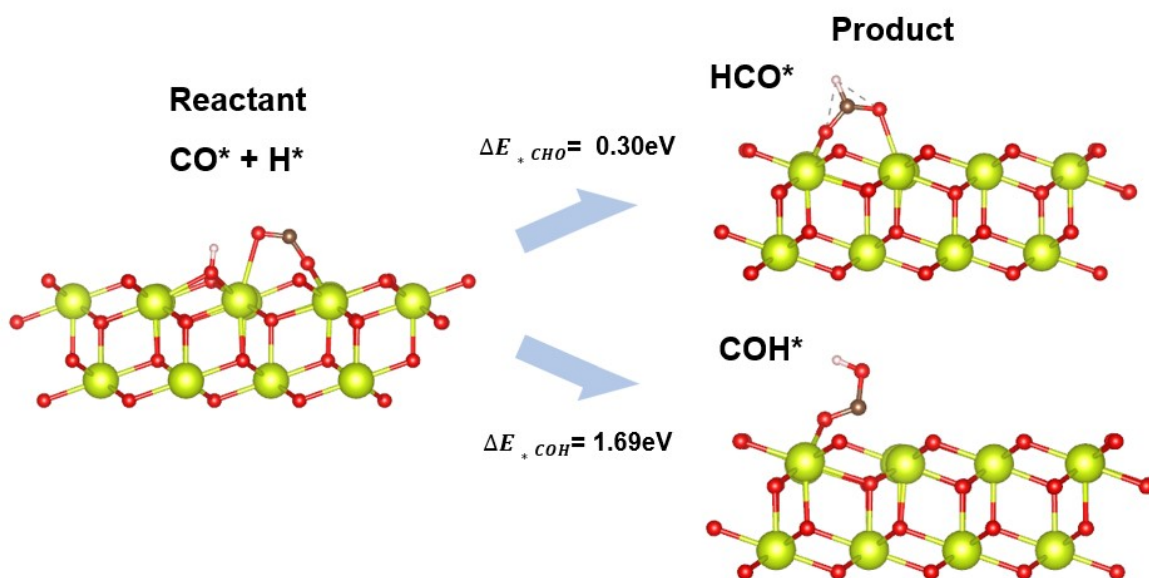


Fig. S23. CO hydrogenation energy on CeO_2 was calculated via the reaction energy of $\text{CO}^* + \text{H}^* \rightarrow \text{HCO}^*$ or COH^* .

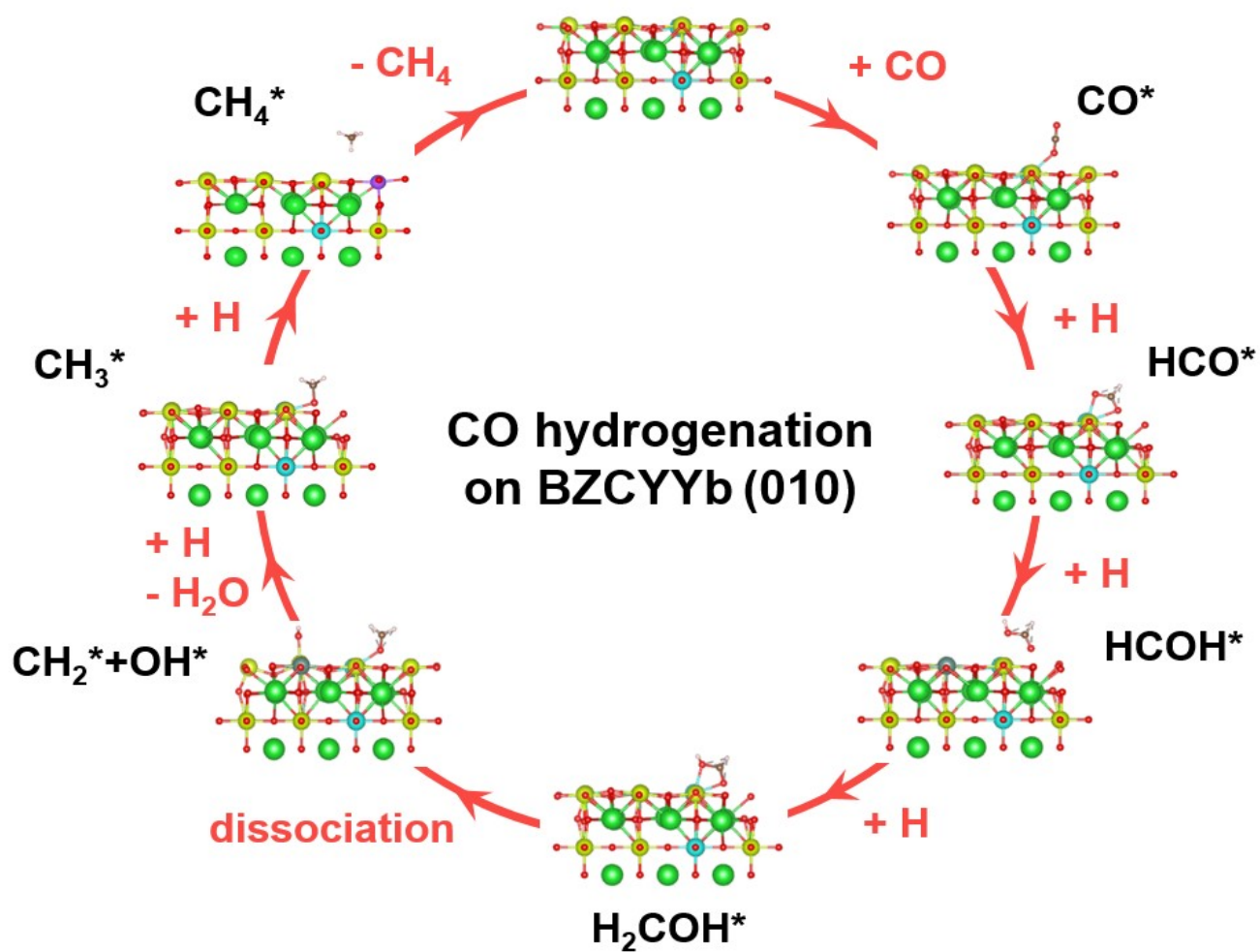


Fig. S24. All configurations of the adsorbed intermediates on BZCYYb. The H atoms come from electrochemically driven surface reaction intermediates.



Fig. S25. All configurations of the adsorbed intermediates on CeO₂. The H atoms come from electrochemically driven surface reaction intermediates.

Table S4. The reaction energy of each step in CO hydrogenation reaction.

Reaction	Reaction formula	CeO ₂ (eV)	BZCYYb (eV)
CO hydrogenation	CO*+6H* → HCO*+5H*	0.30	0.84
HCO hydrogenation	HCO*+5H* → HCOH*+4H*	1.76	1.19
HCOH hydrogenation	HCOH*+4H* → H ₂ COH*+3H*	0.38	1.58
H ₂ COH dissociation	H ₂ COH*+3H* → CH ₂ *+OH*+3H*	1.52	0.95
water desorption & CH ₂ formation	CH ₂ *+OH*+3H* → CH ₂ * +H ₂ O(g) +2H*	-0.34	0.69
CH ₃ formation	CH ₂ * +2H* → CH ₃ *+H*	-0.27	1.54
CH ₄ formation	CH ₃ * +H* → CH ₄ *	1.25	2.50

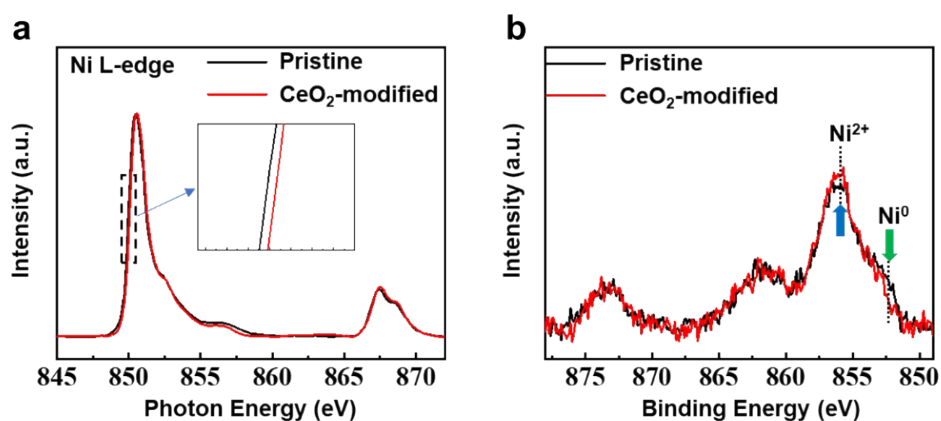


Fig. S26. (a) Ni L-edge X-ray-absorption spectra, (b) Ni 2p XPS spectra for the pristine (black) and CeO₂-modified (red) electrodes.

References

1. X. Li, K. Blinn, D. Chen and M. Liu, *Electrochem. Energy Rev.*, 2018, **1**, 433-459.
2. J. H. Kim, Z. Y. Chern, S. Yoo, B. deGlee, J. Wang and M. Liu, *ACS Appl Mater Interfaces*, 2020, **12**, 2370-2379.
3. J. H. Kim, M. Liu, Y. Chen, R. Murphy, Y. Choi, Y. Liu and M. Liu, *ACS Catalysis*, 2021, **11**, 13556-13566.
4. A. S. Varela, W. Ju, T. Reier and P. Strasser, *ACS Catalysis*, 2016, **6**, 2136-2144.
5. A. S. Varela, N. Ranjbar Sahraie, J. Steinberg, W. Ju, H. S. Oh and P. Strasser, *Angew. Chem. Int. Ed. Engl.*, 2015, **54**, 10758-10762.
6. M. Zhou, J. Liu, Y. Ye, X. Sun, H. Chen, D. Zhou, Y. Yin, N. Zhang, Y. Ling, F. Ciucci and Y. Chen, *Small*, 2021, **17**, e2104144.
7. R. O'Hayre, S.-W. Cha, W. Colella and F. B. Prinz, *Fuel cell fundamentals*, John Wiley & Sons, 2016.
8. C. Duan, J. Huang, N. Sullivan and R. O'Hayre, *Applied Physics Reviews*, 2020, **7**, 011314.
9. H. Zhu, S. Ricote, C. Duan, R. P. O'Hayre and R. J. Kee, *Journal of The Electrochemical Society*, 2018, **165**, F845-F853.

10. J. Pan, Y. Ye, M. Zhou, X. Sun and Y. Chen, *Energy & Fuels*, 2022, **36**, 12253-12260.
11. E. Vollestad, R. Strandbakke, M. Tarach, D. Catalan-Martinez, M. L. Fontaine, D. Beeaff, D. R. Clark, J. M. Serra and T. Norby, *Nat. Mater.*, 2019, **18**, 752-759.
12. Z. Pan, C. Duan, T. Pritchard, A. Thatte, E. White, R. Braun, R. O'Hayre and N. P. Sullivan, *Applied Catalysis B: Environmental*, 2022, **307**, 121196.
13. N. Shi, Y. Xie, D. Huan, Y. Yang, S. Xue, Z. Qi, Y. Pan, R. Peng, C. Xia and Y. Lu, *J. Mater. Chem. A*, 2019, **7**, 4855-4864.
14. K. Xie, Y. Zhang, G. Meng and J. T. S. Irvine, *J. Mater. Chem.*, 2011, **21**, 195-198.
15. T. Pu, W. Tan, H. Shi, Y. Na, J. Lu and B. Zhu, *Electrochim. Acta*, 2016, **190**, 193-198.
16. G. Wu, K. Xie, Y. Wu, W. Yao and J. Zhou, *J. Power Sources*, 2013, **232**, 187-192.
17. F. Liu, L. Fang, D. Diercks, P. Kazempoor and C. Duan, *Nano Energy*, 2022, **102**.
18. E. Ruiz-Trejo and J. T. S. Irvine, *Solid State Ionics*, 2013, **252**, 157-164.
19. N. Danilov, A. Tarutin, J. Lyagaeva, G. Vdovin and D. Medvedev, *J. Mater. Chem. A*, 2018, **6**, 16341-16346.
20. C. Duan, R. Kee, H. Zhu, N. Sullivan, L. Zhu, L. Bian, D. Jennings and R. O'Hayre, *Nat. Energy*, 2019, **4**, 230-240.
21. L. Chen, F. Chen and C. Xia, *Energy Environ. Sci.*, 2014, **7**, 4018-4022.
22. L. Bian, C. Duan, L. Wang, Y. Hou, L. Zhu, R. O'Hayre and K.-C. Chou, *Journal of The Electrochemical Society*, 2018, **165**, F981-F985.
23. M. Zheng, S. Wang, Y. Yang and C. Xia, *Journal of Materials Chemistry A*, 2018, **6**, 2721-2729.
24. D. J. Deka, S. Gunduz, T. Fitzgerald, J. T. Miller, A. C. Co and U. S. Ozkan, *Applied Catalysis B: Environmental*, 2019, **248**, 487-503.
25. S. Hou and K. Xie, *Electrochimica Acta*, 2019, **301**, 63-68.
26. M. K. Khameneh and A. Babaei, *Electrochimica Acta*, 2019, **299**, 132-142.
27. V. Kyriakou, D. Neagu, E. I. Papaioannou, I. S. Metcalfe, M. C. M. van de Sanden and M. N. Tsampas, *Applied Catalysis B: Environmental*, 2019, **258**.

28. M. Lo Faro, S. C. Zignani, S. Trocino, V. Antonucci and A. S. Aricò, *Electrochimica Acta*, 2019, **296**, 458-464.
29. B. Niu, C. Lu, W. Yi, S. Luo, X. Li, X. Zhong, X. Zhao and B. Xu, *Applied Catalysis B: Environmental*, 2020, **270**.
30. J. Gan, N. Hou, T. Yao, L. Fan, T. Gan, Z. Huang, Y. Zhao and Y. Li, *Catalysis Today*, 2021, **364**, 89-96.
31. Z. Ma, Y. Li, Y. Zheng, W. Li, X. Chen, X. Sun, X. Chen and J. Zhou, *Ceramics International*, 2021, **47**, 23350-23361.
32. S. J. Baxter, M. Rine, B. Min, Y. Liu and J. Yao, *Journal of CO₂ Utilization*, 2022, **59**, 101954.
33. P. Błaszczak, M. Zając, A. Ducka, K. Matlak, B. Wolanin, S.-F. Wang, A. Mandziak, B. Bochentyn and P. Jasiński, *International Journal of Hydrogen Energy*, 2022, **47**, 35017-35037.
34. C. Xi, J. Sang, A. Wu, J. Yang, X. Qi, W. Guan, J. Wang and S. C. Singhal, *International Journal of Hydrogen Energy*, 2022, **47**, 10166-10174.
35. J. D. Yi, R. Xie, Z. L. Xie, G. L. Chai, T. F. Liu, R. P. Chen, Y. B. Huang and R. Cao, *Angew. Chem. Int. Ed. Engl.*, 2020, **59**, 23641-23648.
36. G. Shi, Y. Xie, L. Du, X. Fu, X. Chen, W. Xie, T. B. Lu, M. Yuan and M. Wang, *Angew. Chem. Int. Ed. Engl.*, 2022, **61**, e202203569.
37. Y. Cai, J. Fu, Y. Zhou, Y. C. Chang, Q. Min, J. J. Zhu, Y. Lin and W. Zhu, *Nat. Commun.*, 2021, **12**, 586.
38. Q. Hu, Z. Han, X. Wang, G. Li, Z. Wang, X. Huang, H. Yang, X. Ren, Q. Zhang, J. Liu and C. He, *Angew. Chem. Int. Ed. Engl.*, 2020, **59**, 19054-19059.
39. Z. H. Zhao, J. R. Huang, P. Q. Liao and X. M. Chen, *Angew. Chem. Int. Ed. Engl.*, 2023, DOI: 10.1002/anie.202301767, e202301767.
40. Z. Weng, Y. Wu, M. Wang, J. Jiang, K. Yang, S. Huo, X. F. Wang, Q. Ma, G. W. Brudvig, V. S. Batista, Y. Liang, Z. Feng and H. Wang, *Nat. Commun.*, 2018, **9**, 415.

41. Y. Wang, Z. Chen, P. Han, Y. Du, Z. Gu, X. Xu and G. Zheng, *ACS Catalysis*, 2018, **8**, 7113-7119.
42. L. Han, X. Liu, J. He, Z. Liang, H. T. Wang, S. M. Bak, J. Zhang, A. Hunt, I. Waluyo, W. F. Pong, J. Luo, Y. Ding, R. R. Adzic and H. L. Xin, *Advanced Energy Materials*, 2021, **11**, 2100044.
43. C. J. Chang, S. C. Lin, H. C. Chen, J. Wang, K. J. Zheng, Y. Zhu and H. M. Chen, *J. Am. Chem. Soc.*, 2020, **142**, 12119-12132.
44. L. Han, S. Song, M. Liu, S. Yao, Z. Liang, H. Cheng, Z. Ren, W. Liu, R. Lin, G. Qi, X. Liu, Q. Wu, J. Luo and H. L. Xin, *J. Am. Chem. Soc.*, 2020, **142**, 12563-12567.
45. H. Zhang, X. Chang, J. G. Chen, W. A. Goddard, 3rd, B. Xu, M. J. Cheng and Q. Lu, *Nat. Commun.*, 2019, **10**, 3340.
46. H. S. Jeon, J. Timoshenko, F. Scholten, I. Sinev, A. Herzog, F. T. Haase and B. Roldan Cuenya, *J. Am. Chem. Soc.*, 2019, **141**, 19879-19887.
47. D. Ren, J. Fong and B. S. Yeo, *Nat. Commun.*, 2018, **9**, 925.
48. L. Lin, T. Liu, J. Xiao, H. Li, P. Wei, D. Gao, B. Nan, R. Si, G. Wang and X. Bao, *Angew. Chem. Int. Ed. Engl.*, 2020, **59**, 22408-22413.
49. Y. Liu, S. Li, L. Dai, J. Li, J. Lv, Z. Zhu, A. Yin, P. Li and B. Wang, *Angew. Chem. Int. Ed. Engl.*, 2021, **60**, 16409-16415.
50. D. Zagoraios, C. Panaritis, A. Krassakopoulou, E. A. Baranova, A. Katsaounis and C. G. Vayenas, *Appl. Catal. B-Environ.*, 2020, **276**, 119148.
51. Y. Wang, H. Zhang, J. Cao, K. Xu, K. Pei and Y. Chen, *Journal of Power Sources*, 2022, **524**.